Identification of regulators of cancer: immune interactions

Logtenberg, M.E.W.

5

QPCTL regulates macrophage and monocyte abundance and inflammatory signatures in the tumor microenvironment

Meike E. W. Logtenberg[1#], Kaspar Bresser[1#], Mireille Toebes[1], and Ton N. Schumacher[1,2]

Manuscript under review

[1] Division of Molecular Oncology & Immunology, Oncode Institute, The Netherlands Cancer Institute, Amsterdam, The Netherlands
[2] To whom correspondence should be addressed at t.schumacher@nki.nl
[#] These authors contributed equally

ABSTRACT

The enzyme glutaminyl-peptide cyclotransferase-like protein (QPCTL) catalyzes the formation of pyroglutamate residues at the NH_2-terminus of proteins, thereby influencing their biological properties. A number of studies have implicated QPCTL in the regulation of chemokine stability. Furthermore, QPCTL activity has recently been shown to be critical for the formation of the high affinity SIRPα binding site of the CD47 "don't-eat-me" protein. Based on the latter data, interference with QPCTL activity—and hence CD47 maturation—may be proposed as a means to promote anti-tumor immunity. However, the pleiotropic activity of QPCTL makes it difficult to predict the effects of QPCTL inhibition on the tumor microenvironment (TME). Using a QPCTL-deficient mouse model, we here demonstrate that QPCTL deficiency on host cells and tumor cells results in a macrophage-biased tumor microenvironment. Furthermore, we demonstrate that prevention of QPCTL activity results in an increased IFN and decreased TGF-ß signature in tumor cells, and a skewing towards pro-inflammatory over immunosuppressive, TGF-ß1-driven, cancer-associated fibroblasts. Collectively, these data provide support for the development of strategies to interfere with QPCTL activity as a means to promote tumor-specific immunity.

INTRODUCTION

Regulation of immune cell activity at sites of infection or cancer growth frequently occurs through a balance of signals that are received by immune activating and immune inhibitory receptors[1]. For example, the activation of myeloid cells, including neutrophils, macrophages and monocytes, often occurs through Fc receptor signaling. Conversely, such activation can be prevented through the simultaneous engagement of ITIM/ITSM-containing inhibitory receptors such as SIRPα. Specifically, binding of the "don't-eat-me" signal CD47, which is widely expressed on hematopoietic and non-hematopoietic cells, to the SIRPα receptor on myeloid cells has been shown to result in decreased myeloid effector function, including suppression of target cell phagocytosis by macrophages and tumor cell killing by neutrophils[2–4].

The inhibitory capacity of CD47 is dependent on the maturation of its SIRPα binding site by the ER-resident enzyme QPCTL[5,6]. Similar to its secreted family member QPCT, QPCTL catalyzes the cyclization of N-terminal glutamine and glutamic acid residues on target proteins into a pyroglutamate residue (pGlu)[7,8]. As shown by structural analysis, the pGlu residue at the N-terminus of CD47 contributes to the interaction surface with SIRPα[9]; and, through genetic screening, it was shown that the activity of QPCTL is critical for the formation of this residue, making this enzyme a key regulator of the high-affinity CD47-SIRPα binding site[6]. In line with this, prevention of pGlu formation on CD47, either by genetic knock-out or small molecule inhibition, leads to reduced SIRPα binding and increased macrophage- and neutrophil-dependent killing of antibody-opsonized target cells. Based on its role in regulating CD47-SIRPα signaling, and the possibility to develop small molecule inhibitors of enzymatic activity, QPCTL forms a potentially interesting target in cancer immunotherapy.

In addition to CD47, the chemokines CCL2 and CX_3CL1 have been identified as QPCTL and/or QPCT substrates[10–12]. The formation of the N-terminal pGlu on CCL2 was shown to increase its *in vivo* activity, both by conferring resistance to aminopeptidases and by increasing its capacity to induce CCR2 signaling[10]. Likewise, pGlu-modified CX_3CL1 appears to show an increased capacity to promote CX_3CR1 signaling *in vitro*[12]. Finally, around 600 human proteins harbor a N-terminal glutamine or glutamic acid residue after the predicted signal peptide cleavage site, and it is plausible that additional QPCTL/QPCT substrates exist amongst this group of proteins[13].

Because of its known or potential role in the post-translational modification of different immune- or tumor cell-related molecules, it is difficult to predict the overall effects of QPCTL inhibition on the tumor microenvironment (TME), and the poor pharmacokinetics of available QPCT/QPCTL inhibitors such SEN177[6] has precluded evaluation by small-molecule inhibition. To address this question, we have generated a QPCTL-deficient mouse model and combined it with QPCTL-deficient tumor cells, to

map the effects of QPCTL deficiency on either cellular compartment on the composition of the TME. The obtained data reveal that QPCTL deficiency results in a skewing of the macrophage-monocyte ratio, and shifts tumor cells from a TGF-ß-responding to an IFN-responding state. Furthermore, we uncover a profound change in the balance between TGF-ß-producing myofibroblastic cancer-associated fibroblasts (myCAFs) and cytokine-secreting inflammatory CAFs (iCAFs), signifying a pro-inflammatory environment. Together, these results suggest that therapeutic manipulation of QPCTL activity may potentially be used to skew the TME to a pro-inflammatory state.

RESULTS

QPCTL-deficiency alters macrophage-monocyte-ratios in the TME

While QPCTL-deficient mouse models have been generated[10,14], the possible effects of QPCTL inactivation on TME composition have not been studied. To determine how blockade of QPCTL activity alters the TME, we generated a QPCTL-deficient ($QPCTL^{-/-}$) mouse model through CRISPR-Cas9 mediated gene-editing. To first determine whether QPCTL deficiency results in abrogation of pGlu formation on CD47, peripheral blood cells from $QPCTL^{-/-}$ mice and WT littermates were stained with mouse SIRPα and an anti-mouse CD47 antibody that recognizes CD47 independent of pyroglutamate formation[6]. As compared to WT littermates, blood cells of QPCTL deficient mice displayed significantly decreased SIRPα binding, thereby providing the first evidence that QPCTL is also a critical CD47 modifier *in vivo* (Fig. 1a-b).

To understand how QPCTL deficiency influences steady-state immune cell frequencies and gene expression, $QPCTL^{-/-}$ and $QPCTL^{+/+}$ littermates were subjected to histopathological, transcriptomic and flow cytometric analysis. Histopathological assessment of $QPCTL^{-/-}$ mice revealed no significant morphological aberrations relative to littermate controls (Supplementary Data 1), and gene expression analysis of spleen, lymph nodes and bone marrow revealed no genotype-specific transcriptional changes (Fig. 1c, Extended Data Fig. 1a), indicating that QPCTL deficiency does not result in major alterations in steady-state immune activity. Likewise, no substantial differences in cell counts or immune cell population frequencies were observed in blood (Extended Data Fig. 1b-c). In spleen, a modest increase in the frequency of NK cells of total non-myeloid cells and a decrease in the fraction of activated cells of total $CD4^+$ T cells was observed in $QPCTL^{-/-}$ mice, but no significant changes in other immune cell type frequencies were identified (Extended Data Fig. 1d). The absence of substantial differences in immune cell frequencies was corroborated by unbiased hierarchical clustering of cells obtained from $QPCTL^{+/+}$ and $QPCTL^{-/-}$ spleen samples (Fig. 1d and Extended Data Fig. 1e).

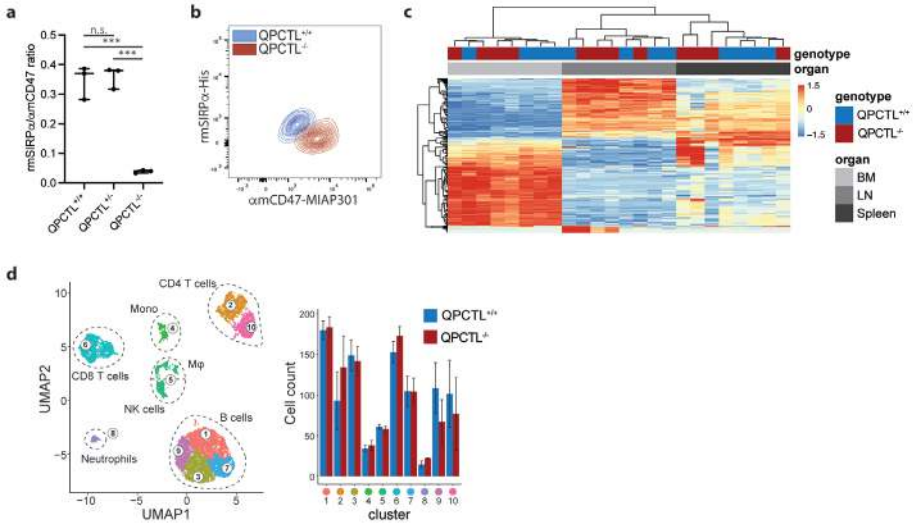

Figure 1. Generation and characterization of QPCTL-deficient mice. a. Ratio of recombinant mouse (rm) SIRPα-His and anti-mouse (am) CD47 antibody (clone MIAP301) binding to blood cells from QPCTL$^{+/+}$, QPCTL$^{+/-}$ and QPCTL$^{-/-}$ mice, as measured by flow cytometry. Data represent median ± min to max of individual mice. Dots depict the ratio of rmSIRPα-His/amCD47-MIAP301 mean fluorescence intensity (MFI) on blood cells from individual mice, n = 3 mice per group. ***P = 0.0002 (QPCTL$^{+/+}$ vs QPCTL$^{-/-}$); ***P = 0.0001 (QPCTL$^{+/-}$ vs QPCTL$^{-/-}$) by one-way ANOVA. n.s., not significant. **b.** Flow cytometry plot depicting data described in a) for blood cells from a representative QPCTL$^{+/+}$ and QPCTL$^{-/-}$ mouse. **c.** Heatmap depicting hierarchical clustering performed on the 1,000 most differentially expressed genes in bone marrow (BM), lymph node (LN) and spleen samples from QPCTL$^{+/+}$ and QPCTL$^{-/-}$ mice. **d.** Unbiased Euclidean distance-based clustering of immune cells obtained from spleens of QPCTL$^{+/+}$ and QPCTL$^{-/-}$ mice. UMAP 2-dimensional projection (left) depicts the obtained clusters. Cell counts of both genotypes within each cluster are depicted (right). Bars indicate group means, error bars represent standard error of the mean. Data in **a**-**b**) are representative of 3 experiments with similar results, data in **c**-**d**) were obtained in a single experiment. UMAP, Uniform Manifold Approximation and Projection.

To test whether systemic QPCTL deficiency influences immune cell infiltration in the TME, QPCTL$^{+/+}$ and QPCTL$^{-/-}$ mice were inoculated with wild-type and QPCTL-deficient B16F10 melanoma cells, respectively (Extended Data Fig. 2a). Analysis of TMEs 14-16 days after tumor inoculation revealed a high frequency of myeloid cells in both wild-type and QPCTL-deficient tumor lesions (Extended Data Fig. 2b-c). Importantly, within the myeloid subset, QPCTL-deficient tumors exhibited a significant higher frequency of macrophages and a substantially increased macrophage-monocyte (Mϕ-Mo) ratio (Fig. 2a). Although no other significant changes within the immune infiltrate could be detected (Extended Data Fig. 2c), an increase in the frequency of B cells, a trend toward a decrease in monocytes, and a decrease in the frequency of CD4^{+} T cells within the non-myeloid immune cell subset was observed in peripheral blood samples from QPCTL-deficient tumor-bearing mice (Extended Data Fig. 2d). Also, when immune infiltrates of QPCTL-deficient and -proficient tumors were analyzed through unbiased hierarchical clustering, an increase in F4/80^{+} cells (macrophages) and a decrease in Ly6C^{high} cells (monocytes) in QPCTL-deficient TMEs was observed (Fig. 2b-c and Extended Data Fig. 2e).

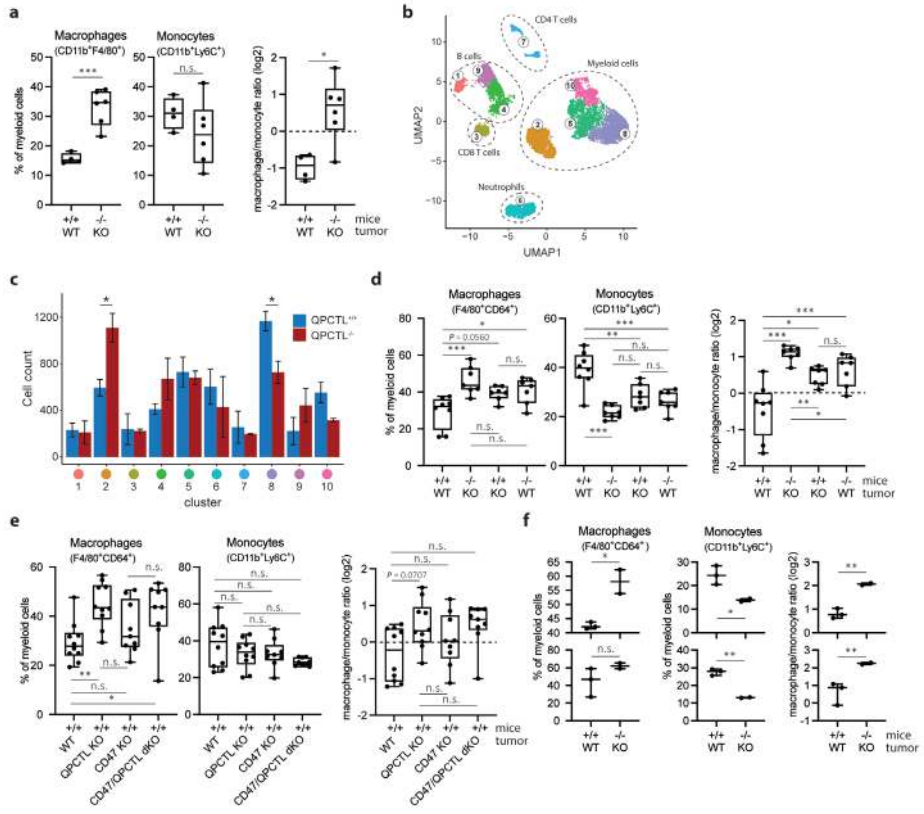

Figure 2. Tumor and host QPCTL deficiency leads to a shift in Mϕ-Mo ratio in the TME. a. Frequency of macrophages ($CD11b^+F4/80^+$) and monocytes ($CD11b^+Ly6C^+$) of myeloid cells ($CD11b^+$), and Mϕ/Mo ratio, in the TME of $QPCTL^{+/+}$ (+/+) and $QPCTL^{-/-}$ (-/-) mice inoculated with B16F10 WT tumor cells and B16F10 QPCTL KO tumor cells, respectively. Data represent median ± min to max of individual mice. Dots depict immune cell frequency (%) or ratio (log_2) within individual mice. $n = 4$ (B16F10 WT tumors in $QPCTL^{+/+}$ mice) and $n = 6$ (B16F10 QPCTL KO tumors in $QPCTL^{-/-}$ mice) mice per group. ***$P = 0.0006$; *$P = 0.0372$; n.s., not significant by unpaired two-tailed *t*-test. **b.** UMAP visualizing 30,000 cells obtained from $QPCTL^{+/+}$ ($n = 3$) and $QPCTL^{-/-}$ ($n = 3$) TMEs. 5,000 cells were randomly drawn from each sample prior to analysis. Colors indicate clusters obtained by Euclidean distance-based hierarchical clustering. **c.** Contribution of cells from $QPCTL^{+/+}$ ($n = 3$) and $QPCTL^{-/-}$ ($n = 3$) TMEs to each cluster. Bars indicate group means; error bars represent standard error of the mean. *P =0.033 (cluster 2); *$P = 0.026$ (cluster 8) by unpaired two-tailed *t*-test. **d.** Frequency of macrophages ($F4/80^+CD64^+$) and monocytes ($CD11b^+Ly6C^+$) of myeloid cells ($CD11b^+$), and Mϕ-Mo ratio, in the TME of $QPCTL^{+/+}$ (+/+) mice inoculated with B16F10 WT or QPCTL KO tumor cells, and in $QPCTL^{-/-}$ (-/-) mice inoculated with B16F10 WT or QPCTL KO tumor cells. Data represent median ± min to max of individual mice. Dots depict immune cell frequency (%) or ratio (log_2) within individual mice. $n = 8$ ($QPCTL^{+/+}$ with WT tumor cells) or $n = 7$ ($QPCTL^{-/-}$ with QPCTL KO tumor cells; $QPCTL^{+/+}$ with QPCTL KO tumor cells; $QPCTL^{-/-}$ with WT tumor cells) mice per group. For macrophages, ***$P = 0.0006$; *$P = 0.0236$; n.s., not significant, by one-way ANOVA. For monocytes, ***$P < 0.0001$ ($QPCTL^{+/+}$ with WT tumor cells vs $QPCTL^{-/-}$ with QPCTL KO tumor cells); ***$P = 0.0004$ ($QPCTL^{+/+}$ mice with WT tumor cells vs $QPCTL^{+/+}$ with QPCTL KO tumor cells); **$P = 0.0030$; n.s., not significant, by one-way ANOVA. For macrophage/monocyte ratio, *$P = 0.0188$ ($QPCTL^{+/+}$ with WT tumor cells vs $QPCTL^{-/-}$ with WT tumor cells); *$P = 0.0304$ ($QPCTL^{-/-}$ mice with WT tumor cells vs $QPCTL^{-/-}$ mice with QPCTL KO tumor cells); n.s., not significant, by one-way ANOVA. **e.** Frequency of macrophages ($F4/80^+CD64^+$) and monocytes ($CD11b^+Ly6C^+$) of myeloid cells ($CD11b^+$), and Mϕ-Mo ratio, in the TME of $QPCTL^{+/+}$ mice inoculated with B16F10 WT, QPCTL KO, CD47 KO, or CD47/QPCTL double-KO (dKO) tumor cells. Data represent median ± min to max of individual mice. Dots depict immune cell frequency (%) or ratio (log_2) within individual mice. $n = 10$ (WT and QPCTL KO tumor cells) or $n = 9$ (CD47 KO and CD47/QPCTL dKO tumor cells) mice per group. **P = 0.0084; *$P = 0.0483$; n.s., not significant, all by one-way ANOVA. **f.** Frequency of macrophages ($F4/80^+CD64^+$) and monocytes ($CD11b^+Ly6C^+$) of myeloid cells ($CD11b^+$), and Mϕ/Mo ratio, in the TME of $QPCTL^{+/+}$ and $QPCTL^{-/-}$ mice inoculated with MC38

WT and MC38 QPCTL KO cells, respectively. The two rows represent two independent experiments. Data represent median ± min to max of individual mice. Dots depict immune cell frequency (%) or ratio (log_2) within individual mice. $n = 3$ ($QPCTL^{+/+}$ with WT tumor cells) or $n = 2$ ($QPCTL^{-/-}$ with QPCTL KO tumor cells) mice per group in each independent experiment. $*P = 0.0176$ (macrophages); $*P = 0.0392$ (monocytes); $**P = 0.0018$ (monocytes); $**P = 0.0015$ (ratio; upper graph) or 0.0075 (ratio; lower graph); n.s., not significant, by unpaired two-tailed *t*-test. Data in a) and d) depict single experiments, and are representative of 3 ($QPCTL^{+/+}$ with WT tumor cells and $QPCTL^{-/-}$ with QPCTL KO tumor cells groups) or 2 ($QPCTL^{+/+}$ with QPCTL KO tumor cells and $QPCTL^{-/-}$ with WT tumor cells groups) independent experiments with similar results. Data in **b**, **c** and **e**) were obtained in a single experiment. Data in **f**) were obtained in 2 independent experiments and are both depicted. Mϕ, macrophages; Mo, monocytes; TME, tumor microenvironment; WT, wild-type; KO, knock-out; dKO, double knock-out.

To determine whether the increased Mϕ-Mo-ratio could be attributed to a lack of QPCTL activity in either host or tumor cells, $QPCTL^{+/+}$ and $QPCTL^{-/-}$ mice were inoculated with either QPCTL-proficient or -deficient melanoma tumor cells (Extended Data Fig. 3a). Both tumor and host QPCTL deficiency led to an increased Mϕ-Mo-ratio, but the most profound increase in Mϕ-Mo-ratios was observed when QPCTL activity was lacking in both cell compartments (Fig. 2d, Extended Data Fig. 3b-c). In blood, the most pronounced differences in immune cell frequencies were found when comparing tumor-bearing versus non-tumor-bearing animals—independent of QPCTL activity—emphasizing that QPCTL deficiency does not impact the systemic immune compartment in a major way (Extended Data Fig. 3d). To explore to what extent loss of pGlu-modified CD47 contributed to the altered intra-tumoral Mϕ-Mo balance, wild-type mice were inoculated with QPCTL-, CD47- or double-deficient tumor cells. Absence of CD47 resulted in Mϕ frequencies that were numerically higher than observed in recipients of WT B16 tumor cells but lower than observed in recipients of QPCTL-deficient cells (Fig. 2e), suggesting that the TME-remodeling effect of QPCTL activity in tumor cells depends, at least in part, on its role as a CD47 modifier.

To test whether the role of QPCTL as a modifier of the TME extended to other tumor models, $QPCTL^{+/+}$ and $QPCTL^{-/-}$ mice were inoculated with QPCTL-proficient- and QPCTL-deficient MC38 colon carcinoma cells, respectively. Following tumor outgrowth, a profound increase in Mϕ-Mo-ratio was observed in QPCTL-deficient TMEs (Fig. 2f, Extended Data Fig. 4a-b), while no significant changes were detected in other immune cell subsets (data not shown). Together, these data indicate that QPCTL affects the TME composition in at least two different tumor models, and that combined tumor and host QPCTL deficiency leads to a significant increase in Mϕ-Mo-ratio.

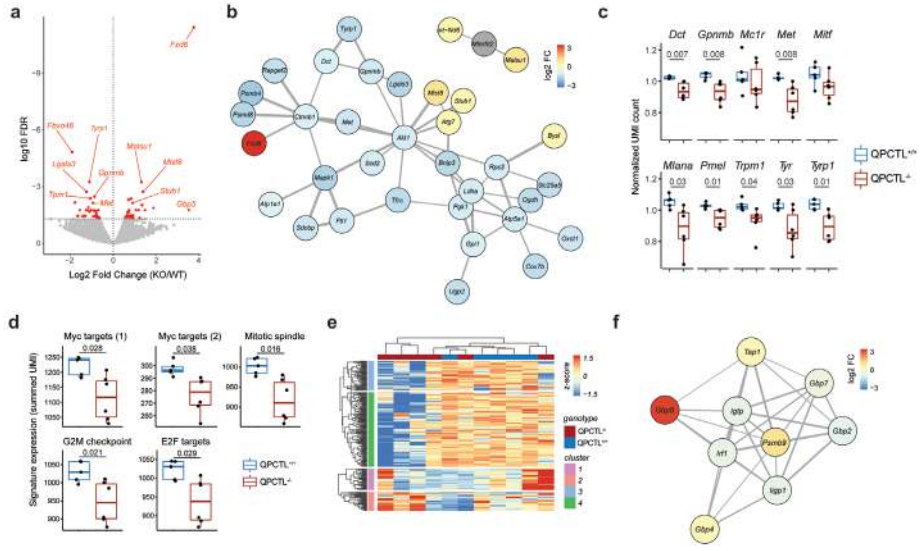

Figure 3. QPCTL-deficiency results in suppression of melanogenesis and cell metabolism. a. Differential gene expression analysis represented as a volcano plot. Genes with an FDR < 0.05 are indicated in red. Selected genes are indicated. **b.** Network analysis (StringDB) performed on all significantly differentially expressed genes. Genes with a medium interaction strength (> 0.4) are included. Line thickness indicates interaction strength. Nodes are colored based on log2 fold differences obtained in panel a. **c.** Boxplots depicting expression of selected genes in the melanogenesis pathway in QPCTL$^{+/+}$ (n = 5) and QPCTL$^{-/-}$ (n = 6) TMEs. Center lines signify the median, whiskers represent 1.5 * IQR. **d.** Boxplots depicting expression of cell cycle-associated Hallmark signatures (MsigDB). Signature expression is calculated as the sum of normalized UMI counts of genes within each signature. Dots depict data from individual QPCTL$^{+/+}$ (n = 5) and QPCTL$^{-/-}$ (n = 6) TMEs. Center lines signify the median, whiskers represent 1.5 * IQR. **e.** Heatmap summarizing hierarchical clustering of the 1,000 most differentially expressed genes across QPCTL$^{+/+}$ (n = 5) and QPCTL$^{-/-}$ (n = 6) TMEs. (**f**) Network analysis (StringDB) performed on cluster 2 genes (panel e). Genes with a medium interaction strength (> 0.4) are included. Line thickness indicates interaction strength. Nodes are colored based on $\log_2$ fold differences obtained in panel a. Data in **a**-**f**) are representative of 2 independent experiments. UMI, unique molecular identifier. Significant (< 0.05) P values obtained by Tukey's HSD post-hoc test are indicated in the plots. IQR, Interquartile range; MsigDB, Molecular Signatures Database.

QPCTL deficiency is associated with suppressed intra-tumoral melanogenesis and cell metabolism

Having established that QPCTL deficiency is associated with an alteration in intra-tumoral immune cell composition, we set out to investigate the effect of QPCTL deficiency on the tumor cell and stromal cell compartment of the TME. RNA sequencing of CD45-negative cell fractions from QPCTL deficient- and proficient TMEs showed that QPCTL deficiency resulted in differential expression of a substantial set of genes (Fig. 3a, Extended Data Fig. 5a), and network analysis revealed that expression of multiple genes involved in melanogenesis (*Dct*, *Tyrp1*, *Gpnmb*) was reduced in QPCTL-deficient melanomas (Fig. 3b). Assessment of the expression level of a broader set of genes involved in melanogenesis likewise showed dampening of this pathway (Fig. 3c). Interestingly, these transcriptional changes coincided with the functional abrogation of melanin production, as

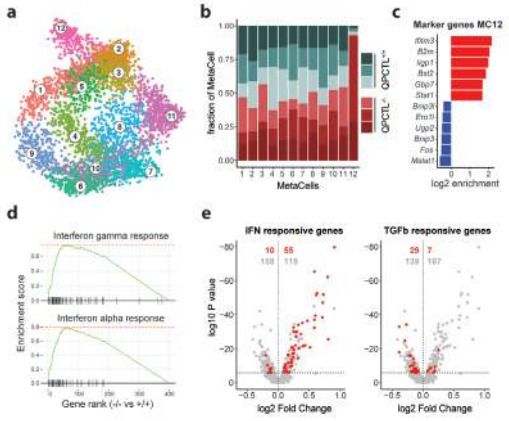

Figure 4. QPCTL deficiency leads to an increased IFN- and decreased TGF-ß-responding transcriptional signature in tumor cells. a. 2-dimensional MetaCell projection of the tumor cell compartment. Single cells are colored by MetaCell. **b**. Stacked barchart depicting the fraction of tumor cells derived from QPCTL$^{+/+}$ (n = 3) or from QPCTL$^{-/-}$ (n = 3) TMEs, for each MetaCell. **c**. Log_2 enrichment of marker genes (top 6 highest and lowest expressed) in tumor cell MetaCell 12. **d.** Enrichment plots for the IFNγ and IFNα response gene sets. **e**. Differential gene expression analysis comparing tumor cells derived from QPCTL$^{+/+}$ and QPCTL$^{-/-}$ TMEs. Results are depicted as volcano plots, the dotted horizontal line indicates an adjusted P value cutoff of 0.05. IFN (left) or TGFb (right) signature genes are highlighted in red. Red numbers denote quantity of significant differentially expressed genes within the signature, grey numbers denote the quantity of remaining differentially expressed genes. Data in **a**-**e**) represent data acquired from 6 individual TMEs (3 QPCTL$^{+/+}$; 3 QPCTL$^{-/-}$) obtained in a single experiment.

evidenced by the loss of pigmentation of QPCTL-deficient tumors (Extended Data Fig. 5b). Furthermore, expression of a network of genes involved in cell cycle (*Mapk1*, *Akt1*) and cell metabolism (*Pgk1*, *Atp5a1*, *Oxct1*) was decreased in QPCTL-deficient CD45-negative cells (Fig. 3b). In line with this observation, the expression of several hallmark gene-sets relating to cellular proliferation were significantly reduced in QPCTL-deficient samples (Fig. 3d, Extended Data Fig. 5c), suggesting dampened proliferative activity. Notably, expression of the transcriptional mediator β-catenin, a central effector protein in the Wnt pathway, was also reduced in QPCTL-deficient CD45-negative cells. β-catenin has previously been implicated as an upstream regulator of both cellular proliferation and the melanogenesis pathway[15,16], suggesting that the decreased expression of genes involved in these pathways may be linked.

To further explore putative transcriptional alterations in the CD45-negative compartment as a result of QPCTL deletion, obtained transcriptomes were clustered based on the top 1,000 most variable genes, revealing a cluster of genes that was moderately enriched in 3 out of 6 QPCTL-deficient samples (gene cluster 2, Fig. 3e). Network analysis performed on this cluster showed that this gene set contained a small network comprised of IFN induced genes (*Gbp* family members, *Tap1*, *Irf1*; Fig. 3f). Interestingly, others have described an interplay between IFN responsive genes and the β-catenin pathway[17–19], a notion that potentially links these two signaling networks.

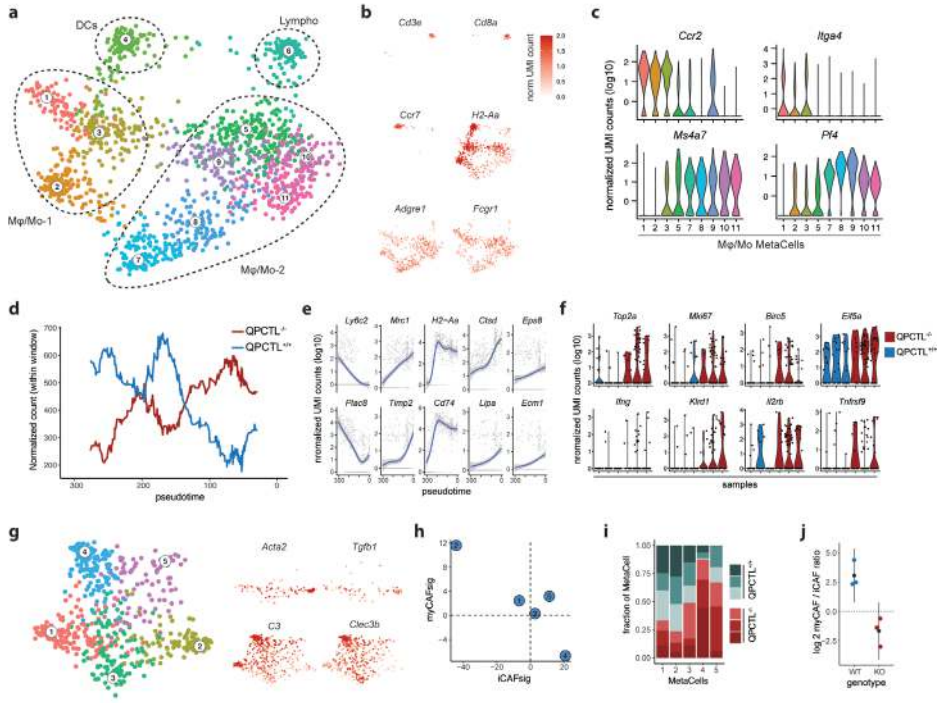

Figure 5. QPCTL deficiency alters the immune cell compartment and CAF polarization in the TME. a. 2-dimensional projection of MetaCell analysis of the immune cell compartment. Single cells are colored by MC. **b.** Normalized UMI count of selected genes superimposed on the 2-dimensional MetaCell projection. **c.** Violin plots depicting normalized UMI counts of selected genes across Mϕ/Mo MCs. (**d-e**) SlingShot Trajectory analysis performed on Mϕ/Mo subset 1 (MC1, 2 and 3). **d.** QPCTL$^{-/-}$ or QPCTL$^{+/+}$ TMEs replicates were pooled, and normalized cell counts were tallied within windows of 60 cell-codes wide, sliding 1 cell-code per frame. Lines indicate normalized cell counts within each window. **e.** Normalized UMI counts of selected genes that are significantly associated with pseudotime. Blue lines indicate general additive linear models, greyed areas indicate confidence intervals, grey dots represent single cells. **f.** Violin plots depicting normalized UMI counts of selected genes within the CD3^{+} lymphoid cell MetaCell (MC6). Expression in QPCTL$^{+/+}$ (n = 3) and QPCTL$^{-/-}$ (n = 3) TMEs is depicted. **g.** 2-dimensional MetaCell projection of the fibroblast compartment. Single cells are colored by MetaCell (left) or normalized UMI count of selected genes (right). **h.** Enrichment of the iCAF and myCAF signatures (Supplementary Table 1) in each MetaCell. Plotted values represent summed log2 transformed enrichment values, calculated by the MetaCell algorithm. **i.** Stacked barchart depicting the fraction of fibroblasts derived from the QPCTL$^{+/+}$ (n = 3) or QPCTL$^{-/-}$ (n = 3) setting, for each MetaCell. **j.** Stripchart depicting the myCAF/iCAF ratio in the QPCTL$^{+/+}$ (n = 3) or QPCTL$^{-/-}$ (n = 3) setting. Colored dots indicate individual mice, black dots indicate means, black bars indicate standard deviation. Data **a**-**j**) represent data acquired from 6 individual TMEs (3 QPCTL$^{+/+}$; 3 QPCTL$^{-/-}$) obtained in a single experiment. iCAF, inflammatory cancer-associated fibroblast; myCAF, myofibroblastic cancer-associated fibroblast.

Single cell transcriptomic profiling reveals remodeling of the tumor micro-environment by QPCTL deficiency

The above data indicate that QPCTL inactivation affects both immune cell composition of the TME and the transcriptome of non-immune cells at the tumor site. With the aim to potentially link these two observations we subsequently performed scRNAseq of both immune cells and non-immune cells from QPCTL-deficient and -proficient TMEs (a total of 13,093 transcriptomes derived from 6 TMEs). Applying the MetaCell algorithm[20], 3 transcriptionally divergent cell supertypes reflecting immune cells (*Ptprc*, *Itgam*), fibroblasts (*Col1a1*, *Acta2*), and tumor cells (*Mlana*, *Pmel*) were distinguished (Extended Data Fig. 6a-c), and to identify cell type-specific changes that accompany QPCTL deficiency, each of these supertypes was re-clustered and analyzed separately.

First, to investigate which of the transcriptional changes observed in the CD45-negative compartment could be mapped to the tumor cell compartment, this supertype was re-grouped into transcriptionally disparate MCs (Fig. 4a, Extended Data Fig. 6d) and the relative contribution of cells from either QPCTL-deficient mice or QPCTL-proficient mice to the different MCs was examined. Strikingly, 1 MC (MC12) was nearly exclusively observed in QPCTL-deficient samples (Fig. 4b). Examination of the marker genes of MC12 showed the presence of a prominent IFN responsive signature (*Ifitm3*, *B2m*, *Bst2*, *H2-D1*; Fig. 4c-d, Extended Data figure 6e-f), and IFN responsive genes were also among the most upregulated genes detected in QPCTL-deficient samples across all MCs (Fig. 4e). MC12 made up approximately 8% of the tumor cell fraction and was predominantly composed of cells derived from 2 of the 3 QPCTL-deficient TMEs. Together with the observations made in the bulk RNAseq dataset (Fig. 3), in which an IFN-signature was observed in half of the QPCTL-deficient samples, these data suggest that QPCTL deficiency increases the probability of tumor cell exposure to IFN in the TME. Next to the increased IFN-signature, multiple TGF-β related gene sets showed reduced expression within the QPCTL-deficient tumor cell compartment (Fig 4e, Extended Data figure 6g). Retrospective analysis likewise revealed a negative trend in the expression of genes associated with TGF-β exposure in CD45-negative cells from QPCTL-deficient TMEs in bulk RNAseq data (Extended Data Fig. 6h). Thus, using two independent gene expression datasets, QPCTL inactivation was found to result in a decreased TGF-ß- and an increased IFN-responding gene signature within the tumor cell compartment.

Next, the immune cell compartment was grouped into 11 MetaCells (MCs) classified as either $CD3^+$ lymphocytes (*Cd8a*, *Cd3e*), dendritic cells (*Ccr7*, *H2-Aa*), or macrophages/monocytes (*Adgre1*, *Fcgr1*; Fig. 5a-b, Extended Data Fig. 6i). The macrophage/monocyte (Mϕ/Mo) MCs could be further subdivided into 2 groups that were marked by high expression of either *Ccr2* and *Itga4* (Mϕ/Mo-1 subgroup) or *Ms4a7 and Pf4*^{HI} (Mϕ/Mo-2 subgroup; Fig. 5b-c), suggestive of a blood- versus tissue-derived origin[21–24]. Analysis of the contribution of cells from QPCTL-deficient and proficient TMEs to individual MCs

indicated that QPCTL deficiency changed the relative abundance of the different cell states that jointly comprised the Mϕ/Mo-1 subgroup (Extended Data Fig. 6j). As intratumoral Mϕ/Mo cells can exist within a continuum of transcriptional cell states[25,26], a pseudotime analysis was subsequently performed on Mϕ/Mo subgroup 1 to examine if such a continuum could be observed, and whether this was linked to QPCTL deficiency. This analysis revealed a strong continuous association between pseudotime (i.e. cell state) and sample-origin (Fig. 5d). To investigate the transcriptional changes underlying this association, genes were clustered based on their expression kinetics across pseudotime (Extended Data Fig. 6k), revealing a gradual loss of expression of Mo-related genes *Ly6c2* and *Plac8* across pseudotime (Fig. 5e), with the lowest expression levels found in the area that contained the highest fraction of cells from QPCTL TMEs. At the same time, an increase in genes linked to 'inflammation-resolutory' Mϕ's (*Mrc1, Timp2*), antigen-presentation (*H2-Aa, Cd74*) and Mϕ effector function (*Eps8*, *Ctsd*, *Ecm1, Lipa*)[27–30] was observed. These observations are consistent with a model in which QPCTL deficiency in the TME leads to transcriptional changes that drive Mo-to-Mϕ conversion, a notion that would fit with the Mϕ-Mo skewing observed using phenotypic markers (Fig. 2).

In line with the flow cytometric analysis, no differences in the frequencies of $CD3^+$ lymphoid cells derived from QPCTL-deficient versus QPCTL-proficient TMEs could be observed in the scRNAseq dataset. However, as activated lymphoid cells are potent producers of IFN, we queried whether transcriptional features associated with lymphocyte activation were detected more frequently in lymphocytes from QPCTL-deficient TMEs. Interestingly, expression of genes associated with TCR-triggering (*Ifng*, *Il2rb* and *Tnfrsf9*) and cell cycle activity (*Top2a*, *Mki67*, *Birc5*) was detected more frequently in cells derived from the QPCTL-deficient tumors (Fig. 5f). Likewise, lymphocytes derived from QPCTL-deficient TMEs showed increased expression of the *Ccl3*, *Ccl4*, and *Ccl5* chemokines, and of the T cell activation-related genes *Ly6a, Nkg7*, and *Gzmb* (Extended Data Fig. 6l). While the increase in *Ifng* gene expression in lymphocytes in QPCTL-deficient samples was only modest, the parallel observation of other aspects of lymphocyte activation in these samples suggests that these cells may, at least in part, be responsible for the IFN responsive signature that is seen in the tumor cell compartment.

Diverse subsets of cancer-cell associated fibroblasts (CAFs) that possess distinct immunomodulatory functions have been reported in the TME of different cancer types[31], and two highly distinctive populations—TGF-β-producing myofibroblastic CAFs (myCAFs) and IL-1-driven inflammatory CAFs (iCAFs)—have been identified in a recent set of cross-species studies[32,33]. As a reduced TGF-β responding signature was identified as one of the characteristics of tumor cells in QPCTL-deficient tumors, we next asked whether QPCTL deficiency affected CAF polarization. MetaCell-based clustering within the fibroblast cell supertype resulted in 5 transcriptionally distinct MCs (Fig 5g, Extended Data figure 6m). Inspection of the marker genes for MC2 (e.g. *Tgfb1* and *Acta2*) and MC4

(e.g. *C3* and *Clec3b*; Fig. 5g) suggested that these cell clusters correspond to TGF-ß-producing myCAFs and IL-1-driven iCAFs[29,30]. In line with this notion, analysis of signature enrichment-scores pertaining to these two subsets showed that MC2 and MC4 scored the highest for either the myCAF or iCAF signature, respectively (Fig. 5h). Strikingly, MC2 and MC4 displayed the highest depletion and enrichment in QPCTL-deficient and -proficient TMEs (Fig. 5i), resulting in a 20-fold increase in the iCAF/myCAF ratio in QPCTL-deficient TMEs (Fig. 5j). Thus, in the absence of QPCTL activity, polarization of fibroblasts toward TGF-β-producing myCAFs is reduced, thereby potentially explaining the dampened TGF-β-responding signature that is found in tumor cells in QPCTL-deficient TMEs.

DISCUSSION

QPCTL activity is known to influence the properties of a number of molecules and may potentially influence additional—as of yet unidentified—substrates. To obtain a global view of the cumulative effects of QPCTL activity on the host's immune response to tumor growth, we made use of a QPCTL-deficient mouse model in combination with syngeneic QPCTL deficient tumor cell lines. We conclude that inactivation of QPCTL alters Mϕ-Mo abundance, increases IFN pathway activity relative to TGF-ß pathway activity, and has a strong effect on the presence of iCAF and myCAF populations in the TME.

The current study has the following limitations: 1) Germline deletion of QPCTL may potentially lead to developmental alterations that influence the host's response to tumor challenge, e.g. affecting the capacity of certain CAF or immune subsets to differentiate, independent of QPCTL activity during tumor growth. However, the absence of obvious phenotypic abnormalities at baseline, and the fact that an increased Mϕ-Mo-ratio was observed in wild-type mice challenged with QPCTL-deficient tumor cells, argue against this possibility. 2) In the present study we have aimed to model the effects of depletion of QPCTL activity on the tumor micro-environment, whereas glutaminyl cyclase inhibitors will, based on the similarity of their active sites, likely inhibit both QPCTL and QPCT activity[34,35]. Such inhibition of QPCT may be relevant as siRNA-mediated suppression of QPCT has been shown to reduce expression of CCL2, CX_3CL1 and CD54/ICAM[12]. In future work, dual inactivation of QPCTL and QPCT may form a means to test this.

The depletion of monocytes that we observe in QPCTL-deficient TMEs may be explained by a decreased functionality of the CCL2-CCR2 signaling axis. In pre-clinical models of breast cancer, the CCL2-CCR2 axis has been shown to influence the abundance of monocytes in primary tumors[36] and metastatic lesions[37]. Furthermore, monocyte recruitment was found to be reduced after thioglycolate challenge of mice that were either QPCTL-deficient or treated with QPCT/QPCTL inhibitors[10]. However, it is important to note that at high concentrations, pyroGlu-CCL2 and unmodified CCL2 demonstrate

similar chemotactic activity[10], and the effect of impaired pyro-glutamylation of CCL2 will therefore depend on local concentrations.

Contrary to expectations, we observed a relative increase in macrophage frequencies in QPCTL-deficient TMEs. Transcriptomic profiling of intra-tumoral Mϕ/Mo cells revealed that these macrophages expressed monocyte-associated molecules (e.g. *Ccr2*, *Itga4*) and pseudotime analysis suggests the existence of intermediate Mϕ-Mo cell states, together arguing in favor of their monocytic origin. In prior work, abrogation of the CCR2-CCL2 signaling axis in monocytes has been shown to strongly reduce the accumulation of intra-tumoral macrophages[38]. Based on these data, we conclude that the boosting of intra-tumoral macrophages by QPCTL inactivation occurs through a mechanism that is independent of CCL2, and is potentially driven by an accelerated monocyte-to-macrophage differentiation program. Moreover, the observation of a numeric increase in Mϕ/Mo-ratio in tumors with a CD47-deficient tumor cell compartment could suggest that the activity of QPCTL as a CD47-modifier contributes to observed the Mϕ/Mo phenotype.

The increased Mϕ-Mo ratio observed in QPCTL-deficient tumors was accompanied by a decreased TGF-ß response signature and an increased IFN response signature in tumor cells. The current data do not distinguish whether these effects are a consequence of myeloid or lymphoid cell-derived IFN. However, the increased expression of activation-associated molecules, such as *Nkg7* and *Ccl5*, in $CD3^+$ lymphocytes in QPCTL-deficient TMEs is consistent with the latter possibility. Notably, TGF-ß can act as a suppressor of IFNγ production by NK cells [39,40], highlighting a possible relationship between these two signatures. In line with these cytokine signatures in tumor cells, we observed a prominent shift in IL-1-iCAF over TGF-ß-myCAF frequencies in QPCTL-deficient TMEs. Notably, in humans, a TGF-ß signature in CAFs is associated with poor responses to anti-PD-L1 in metastatic urothelial cancer[41] and anti-PD-1 treatment in melanoma and NSCLC[42]. Taken together, the shift from an immunosuppressive (TGF-ß) towards a pro-inflammatory (IFN) cytokine profile, and an increased presence of macrophages, in part mediated by loss of CD47 functionality, suggests that QPCTL inactivation biases tumors to a pro-inflammatory state. If this alteration of the TME can also be achieved by pharmacological inhibition of QPCTL in human tumor microenvironments, such inhibitors may potentially synergize with tumor-opsonizing antibodies that rely on the phagocytotic capacity of macrophages—concurrently rewiring the TME to a pro-inflammatory state and relieving inhibitory signaling.

ACKNOWLEDGMENTS

We thank members of the Schumacher lab for discussions and the Netherlands Cancer Institute – Antoni van Leeuwenhoek (NKI/AVL) Transgenic unit, Preclinical Intervention Unit and flow facility for technical support and input. We further thank the NKI animal pathology facility for technical support, and Sjoerd Klarenbeek for histopathological assessment of the QPCTL$^{-/-}$ mice and further input. Lastly, we thank the NKI genomics core facility for processing, and providing input on, sequencing data presented in this work, and for the analysis of the MC38-AMS exome data. This work was supported by ERC AdG SENSIT (grant agreement ID 742259) to T.N.S.

AUTHOR CONTRIBUTIONS

M.E.W.L. and K.B. conceived the project, designed and performed experiments, interpreted data, curated data and co-wrote the manuscript. M.T. designed and performed experiments. T.N.S. conceived the project, designed experiments, interpreted data and co-wrote the manuscript.

COMPETING INTEREST

M.E.W.L. and T.N.S. are inventors on a patent application that covers manipulation of the CD47-SIRPα axis via QPCTL. M.E.W.L. is a consultant for Third Rock Ventures, outside of this work. T.N.S. is advisor to and holds equity in Scenic Biotech that develops QPCTL inhibitors. T.N.S. is consultant for Third Rock Ventures, recipient of grant support from Merck KGaA, and advisor to and stockholder in Allogene Therapeutics, Asher Bio, Merus, and Neogene Therapeutics, all outside of this work.

MATERIAL AND METHODS

Mice

C57/Bl6JR mice were obtained from Janvier. C57/Bl6JRJ QPCTL$^{-/-}$ mice carrying an 811bp deletion in exon 2 of the *Qpctl* gene were derived after introducing Cas9 and a gRNA matching exon 2 of the *Qpctl* gene (5'-GCACAATCAATAAGGGACGC-3') into zygotes. QPCTL$^{-/-}$ mice and QPCTL$^{+/+}$ mice were identified by PCR using the following primers: Fwd_KO (5'-GTTTTAGGGATGGATGCCGC-3'), located before the 811bp deletion, Fwd_WT

(5'-GGACTCCTAGTAGGCAACGG-3'), located in the 811bp deletion, and Rev (5'-GGCTGTTTTGGGATCTTCGG-3'), located after the 811bp deletion.

Evaluation of mouse blood cell counts

Whole blood of mice was collected by heart puncture and total cell counts were determined using a DxH500 Hematology Analyzer (Beckman Coulter).

Blood immune cell preparation

Whole blood of mice was collected into heparin-coated tubes by heart puncture or tail vein puncture at indicated time points. Samples were incubated twice for 5 minutes in erythrocyte-lysis buffer (0.15M NH_4Cl, 10mM $KHCO_3$, 0.1 mM EDTA, pH 7.4), and washed once in staining buffer (0.5% BSA in PBS). Cells were then used for antibody staining, as described below.

Cell lines

B16F10 cells and MC38-AMS cells were kindly provided by D. Peeper (Division of Molecular Oncology & Immunology, Oncode Institute, The Netherlands Cancer Institute, Amsterdam, The Netherlands). The MC38-AMS cell line is a variant of the MC38 cell line available from Kerafast. Whole exome sequencing was performed to compare the MC38-AMS line to the MC38-Kerafast, and has been uploaded to the Sequence Read Archive. B16F10 and MC38-AMS cells were cultured in DMEM (Gibco) supplemented with 10% FCS and penicillin-streptomycin. Cells were cultured at 37 °C and 5% CO_2.

CRISPR/Cas9-mediated generation of CD47 and QPCTL knockout cells

To generate QPCTL- knockout (KO), CD47-KO, and WT control B16F10 cell lines, cells were transfected with pLentiCRISPR v.2 vector encoding sgRNA targeting the murine QPCTL (5'- TATTGATTGTGCGACCCCCG-3') or CD47 (5'- AGCAACAGCGCCGCCGCCAA-3') gene, or left untransfected. Culture medium of transfected cells was supplemented the next day with 2 µg ml^{-1} puromycin for at least 2 days. Selected cells were expanded, and subsequently sorted on the basis of αmCD47-MIAP301^{lo} mSIRPα-Fc^{lo} phenotype (in case of CD47 knockout), or αmCD47-MIAP301^{hi} mSIRPα-Fc^{lo} phenotype (in case of QPCTL knockout), to obtain bulk knockout populations. WT control B16F10 cells were sorted based on morphology gating only. Next, single cells were isolated and expanded, and approximately 50 knockout or wild-type clones were pooled to obtain pure knockout or wild-type populations. To generate CD47/QPCTL double KO (dKO) cell lines, B16F10 QPCTL KO cell lines were transfected with pLentiCRISPR v.2 vector encoding sgRNA targeting the murine CD47 gene. 1 day after transfection, culture medium was supplemented with 2 µg ml^{-1} puromycin for at least 2 days. Single cells were isolated and expanded, and 12 clones were pooled to obtain knockout populations. To generate QPCTL-KO and

control MC38-AMS cell lines, cells were transduced with pLentiCRISPR v.2 vector encoding sgRNA targeting the murine QPCTL gene or a non-targeting control gRNA. 2 days after transduction, culture medium was supplemented with 2 ug ml^{-1} puromycin for at least 4 days. Next, single cells were isolated and expanded, and 12 knock-out (or control) clones were pooled to obtain knockout populations. Gene disruption was validated by sequence analysis of the relevant gene locus by TIDE[44] analysis and, in case of CD47, by flow cytometry.

Tumor challenge

To analyze the effect of QPCTL deficiency in both host and tumor cells or in host cells only, 8 to 25 week-old male and female $QPCTL^{-/-}$ or wild-type $QPCTL^{+/+}$ littermate controls were injected with $2x10^5$ of indicated B16F10 tumor cell lines in 100 μL solution of PBS (Lonza) and Matrigel (Corning) (1:1) in the right flank on day 0. To analyze the effect of tumor cell CD47 deficiency or CD47 and QPCTL-double deficiency, 9–12-week-old C57/Bl6JR (female; Janvier) were injected with $2x10^5$ of indicated B16F10 tumor cell lines. To analyze the effect of QPCTL deficiency in both host and tumor cells in MC38-AMS tumors, 8–25-week-old $QPCTL^{-/-}$ or wild-type $QPCTL^{+/+}$ littermate controls were injected with $5x10^5$ of indicated MC38-AMS tumor cell lines. Tumors were measured 3 times a week, and mice were sacrificed 13-17 days (B16F10 tumors) or 21-29 days (MC38 tumors) after tumor challenge. Mice with a tumor volume equal or below $40mm^3$ were excluded and tumors used for subsequent flow analyses ranged from 75-1436 mm^3 (B16F10 tumors) or 112.5 - 786.5mm^3 (MC38 tumors).

TME single-cell preparation

Tumors were fragmented on ice and were subsequently digested in DMEM (10 ml per tumor) supplemented with collagenase IV (2 mg ml^{-1}, Sigma Aldrich) and DNase I (50 μg ml^{-1}, Sigma Aldrich) for 30 min at 37 °C. Subsequently, 40 ml DMEM supplemented with 10% FCS was added per tumor, and cell suspensions were passed through 100 μm filters. Next, samples were incubated for 5 minutes in erythrocyte-lysis buffer (0.15M NH_4Cl, 10mM $KHCO_3$, 0.1 mM EDTA, pH 7.4), and washed once in staining buffer (0.5% BSA in PBS). Tumor single cell suspensions were then counted and used for antibody staining.

Flow cytometry

Cell surface CD47 was assessed by staining of blood immune cells with the anti-mouse CD47 antibody MIAP301 at a dilution of 1:100 or 1:200 plus His-tagged recombinant mouse SIRPα (rmSIRPα-His) (4, 12 or 36 μg ml^{-1}), in dH_2O (Aqua B. Braun) containing 0.5% (w/v) BSA (Sigma) and 0.2% (w/v) sodium azide (Sigma) (FACS buffer) for 30 min at room temperature, protected from light. After two washes with FACS buffer, cells were stained with a fluorochrome-labeled anti-His antibody at a dilution of 1:100 or 1:200 for

30 min at 4 °C in FACS buffer, while protected from light. Cells were then washed with FACS buffer, and DAPI, propidium iodide, or 7-AAD Viability Staining Solution (eBioscience) was added to allow dead cell exclusion. Antibodies used to analyze immune cells in tumor single cell suspensions are listed in Supplementary Table 2. Measurements were performed on an LSRII, LSRFortessa, or FACSCantoII (BD Biosciences). Data were analyzed using FACS Diva software (BD Biosciences) and FlowJo software.

Unbiased flow cytometry data analysis

Samples were preprocessed using FlowJo software to compensate for spectral overlap, and IR-Dye^{-}CD45^{+} single cells were selected. Further analysis was performed in R, implementing the FlowCore package[45]. Samples were subsampled to obtain 10,000 or 30,000 total cells for spleen or tumor analysis, respectively. Next, a logicle (biexponential) transformation was applied to the measured fluorescence intensities. Uniform Manifold Approximation and Projection (UMAP) was used for dimension reduction, and subsequently used for hierarchical clustering by Euclidean distance (Ward's method). Relative contributions of cells derived from QPCTL$^{-/-}$ and QPCTL$^{+/+}$ samples to each of the clusters was then assessed.

RNA sequencing

RNA was extracted from the indicated frozen tissues using the RNeasy Mini Kit (Qiagen). Flow-sorted cell populations were washed once in PBS, and subsequently lysed in RLT buffer (Qiagen). Whole transcriptome sequencing samples were prepared with the TruSeq Stranded mRNA Kit (Illumina). Paired-end 50 bp sequencing was performed on a NovaSeq 6000 system (S1 flowcell, Illumina), obtaining an average of 18x10^{6} reads per sample. Reads were aligned to the pre-built GRCm38 genome_snp_tran reference using HISAT2[46], and transcript counts were obtained using an in-house generated pipeline (GenSum, https://github.com/NKI-GCF/gensum). Differential gene expression analysis was performed with the edgeR package [47]. Network analysis was performed using the stringDB database, applying the igraph package for visualization.

Single-cell analysis

Single-cell digests of QPCTL$^{-/-}$ and QPCTL$^{+/+}$ TMEs were generated as outlined above. Cells were stained with IR-Dye for dead cell exclusion and with anti-mouse TotalSeq™ Hashtag antibodies (TotalSeq-A0301-06, Biolegend), pooled in equal numbers, and were single-cell sorted on a BD Fusion cell sorter. Single-cell RNA isolation and library preparation was performed according to the manufacturer's protocol of the 10X Genomics Chromium™ Single Cell 3' kit, and the cDNA library was sequenced on the NextSeq™550 Sequencing System (Illumina). A total of ~3.7x10^{8} reads resulted in the detection of 14,888 cells with a median of 3,344 detected genes per cell. Feature-barcode matrices were gen-

erated using the Cell Ranger software of the 10X Genomics Chromium™ pipeline. Further processing was subsequently performed using the MetaCell[20] and Seurat R packages [48]. Cells that contained less than 500 UMIs or had a mitochondrial transcript fraction of > 0.2 were removed. Next, variable genes across the dataset were identified with a normalized variance/mean threshold at 0.1 and a down-sampled coverage threshold at 80, yielding 1,021 genes. These genes were subsequently used as anchors to search for gene-gene correlations across the dataset, and genes with correlations of > 0.1 were included. The obtained genes were then clustered into 50 separate gene-modules, and each was annotated manually.

To identify the major cell types, a feature-gene list was compiled of gene-modules that contained marker genes for various cell type, and these feature-genes were used to generate MetaCells. The obtained MetaCells were then classified as either immune cells, fibroblasts, or tumor cells, as shown in Extended Data Fig. 7. MetaCells that contained significant expression of marker genes from multiple cell types were identified as 'doublet MetaCells', and excluded from further analysis.

Subsequent analysis was performed within each individual cell type. In brief, doublet detection was performed using the HTOdemux function of Seurat, setting the positive quantile at 0.99. Cells containing either a high amount of UMIs or gene-counts were considered doublets and excluded (UMI-thresholds: Immune [10,000], fibroblast [11,000], tumor cell [30,000]; gene-count-threshold: Immune [3,000], fibroblast [4,000], tumor cell [5,700]). Feature genes used for cell type-specific MetaCell generation were obtained using the mcell_gset_filter_varmean and mcell_gset_filter_cov functions implemented in the Metacell package. These features genes were filtered for genes involved in cell cycle (gene-module 7 and 20) and ribosomal proteins (gene-module 2).

For all plots showing normalized UMI counts, a center log ratio normalization was applied, as implemented in the Seurat package [48]. To calculate sample fractions within MetaCells, cell counts were first normalized to 10,000 cells within each sample-hashtag to allow comparison.

Pseudotime analysis was performed using the Slingshot algorithm[49]. Gene-level general additive models were fitted to feature-genes used for MetaCell generation applying the fitGAM function from the TradeSeq R package[50], setting knots at 5. Only genes that associated significantly (adjusted p value < 0.05) with pseudotime were used in subsequent analysis. Genes were then clustered based on expression kinetics across pseudotime based on Euclidean distance. To assess sample composition across pseudotime, the 3 replicates from QPCTL$^{-/-}$ or QPCTL$^{+/+}$ TMEs were analyzed together. To allow pooling of the replicates cell counts were normalized to the total number of cell counts within each sample. Normalized cell counts were then tallied within windows of 60 cell-codes wide, sliding 1 cell-code per frame. Differential gene expression analysis

was performed using the FindMarkers function implemented in Seurat. Wilcoxon Rank Sum test was used to obtain log2 fold changes.

Pathology

For histopathological analyses, 2 µm-thick hematoxylin-eosin stained sections were prepared from formalin-fixed, paraffin-embedded murine tissues, including skin, spleen, thymus, lymph nodes, liver, pancreas, gastrointestinal tract, heart, lung, kidneys, testes, ovaries, accessory sex glands, bone marrow (sternum and extremity), and muscles. Sections were evaluated and scored by an animal pathologist blinded to animal genotype.

Statistical analysis

All statistical analyses were performed either with R (V4.0.5, 'Shake and Throw') or Graphpad (V8.4.1, Prism software). Data are reported as mean ± s.d., as specified. Statistical significance was determined using Student's t-test or one-way analysis of variance (ANOVA), as indicated. All Student's t-tests were two-sided under the assumption of equal variance between samples. All one-way ANOVA tests were corrected for multiple comparisons using statistical hypothesis testing. Differences were considered statistically significant if $P < 0.05$. The n values used to calculate statistics, the type of replicates and the relevant significant P values are noted in the figure legends.

Ethical compliance

All animal experiments were approved by the Animal Welfare Committee of the Netherlands Cancer Institute (NKI), in accordance with national guidelines. All animals were maintained in the animal department of the NKI, housed in individually ventilated cage systems under specific-pathogen-free conditions, and received food and water freely. Mice were used at 8-25 weeks of age.

Data availability

Transcriptomic data presented in the manuscript have been deposited to the Gene Expression Omnibus, and can be accessed as series GSE180201. Exome data for MC38-Kerafast and MC38-AMS have been deposited to the Sequence Read Archive, and can be accessed as project PRJNA753254. R scripts used to produce key figures in the manuscript have been submitted to GitHub (https://github.com/kasbress/QPCTL_analysis).

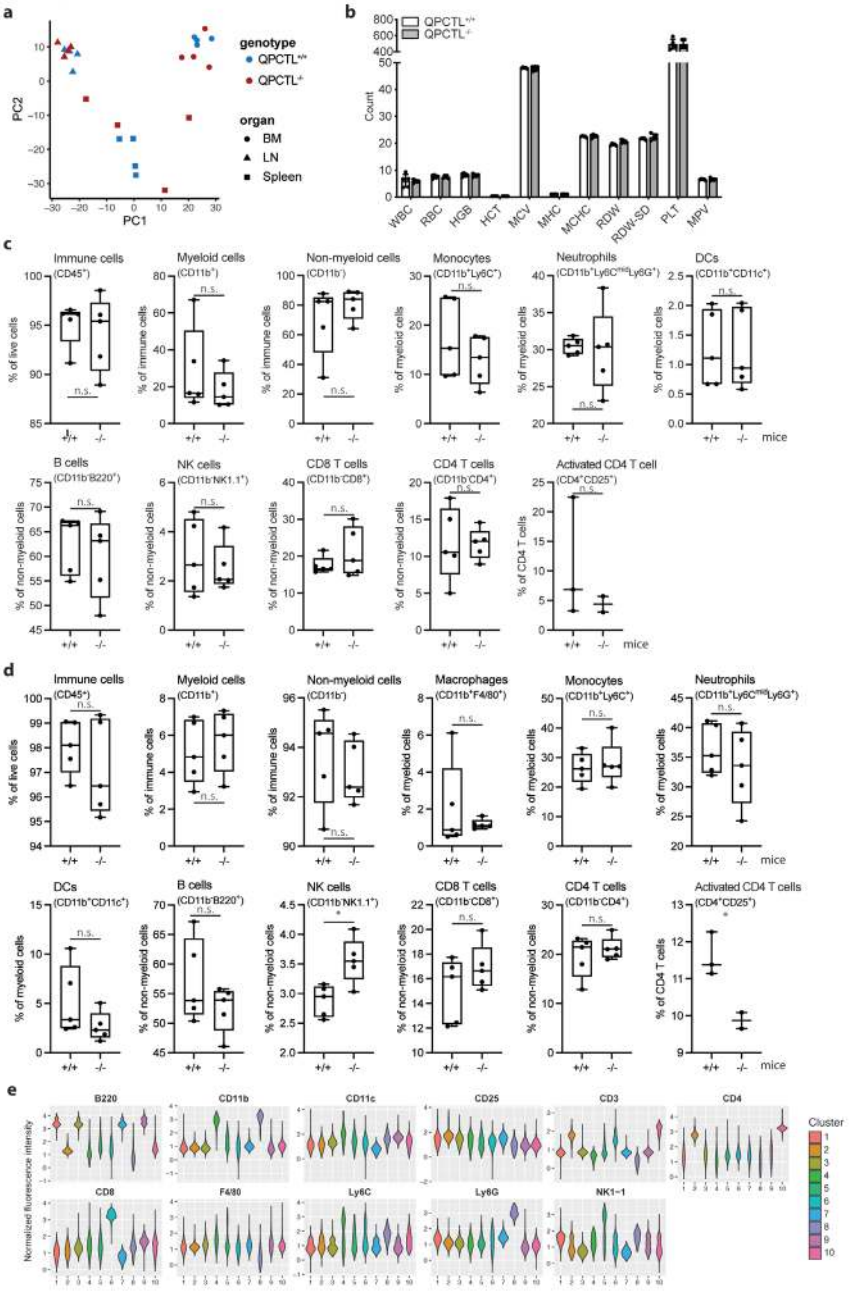

Extended Data Figure 1. Phenotypic analysis of QPCTL KO mice. a. Principal component analysis performed on the 1,000 most differentially expressed genes in bone marrow (BM), lymph node (LN) and spleen samples from QPCTL$^{+/+}$ and QPCTL$^{-/-}$ mice. The first two components are plotted. **b.** Quantification of various components of peripheral blood. Data represent mean ± s.d. of individual mice. Dots depict data from individual mice, n = 5 mice per group. **c.** Frequency of immune cells (CD45^{+}) of total live cells, myeloid (CD11b^{+}) and non-myeloid (CD11b^{-}) cells of immune cells, monocytes

($CD11b^+Ly6C^+$), neutrophils ($CD11b^+Ly6C^{mid}Ly6G^+$) and DCs ($CD11b^+CD11c^+$) of myeloid cells, B cells ($CD11b^-B220^+$), NK cells ($CD11b^-NK1.1^+$), CD8 T cells ($CD11b^-CD8^+$), CD4 T cells ($CD11b^-CD4^+$) of non-myeloid cells, and activated CD4 T cells ($CD4^+CD25^+$) of total CD4 T cells, in blood of $QPCTL^{+/+}$ (+/+) and $QPCTL^{-/-}$ (-/-) mice. Data represent median ± min to max of individual mice. Dots depict immune cell frequency (%) within individual mice. *n* = 3 ($QPCTL^{+/+}$) or *n* = 2 ($QPCTL^{-/-}$) mice per group for activated CD4 T cells; *n* = 5 mice per group for all other immune cell subtypes. n.s., not significant. **d.** Frequency of total immune cells ($CD45^+$) of live cells, myeloid ($CD11b^+$) and non-myeloid ($CD11b^-$) of immune cells, macrophages ($CD11b^+F4/80^+$), monocytes ($CD11b^+Ly6C^+$), neutrophils ($CD11b^+Ly6C^{mid}Ly6G^+$) and DCs ($CD11b^+CD11c^+$) of myeloid cells, B cells ($CD11b^-B220^+$), NK cells ($CD11b^-NK1.1^+$), CD8 T cells ($CD11b^-CD8^+$), CD4 T cells ($CD11b^-CD4^+$) of non-myeloid cells, and activated CD4 T cells ($CD4^+CD25^+$) of total CD4 T cells, in spleen of $QPCTL^{+/+}$ (+/+) and $QPCTL^{-/-}$ (-/-) mice. Data represent median ± min to max of individual mice. Dots depict immune cell frequency (%) within individual mice. *n* = 3 ($QPCTL^{+/+}$) or *n* = 2 ($QPCTL^{-/-}$) mice per group for activated CD4 T cells; *n* = 5 mice per group for all other immune cell subtypes. n.s., not significant. **P* = 0.0115 (NK cells); **P* = 0.0355 (activated CD4 T cells) by unpaired two-tailed *t*-test. n.s., not significant. **e.** Violin plots depicting expression of indicated markers by the cell clusters described in Fig. 1d. Data in **a**-**e**) were obtained in single experiments. Mouse white blood cell, WBC; red blood cell, RBC; hemoglobin, HGB; hematocrit, HCT; mean corpuscular volume, MCV; mean corpuscular hemoglobin. MHC; mean corpuscular hemoglobin concentration, MCHC; red distribution width, RDW; red distribution width - size distribution, RDW-SD; platelet, PLT; mean platelet volume, PV.

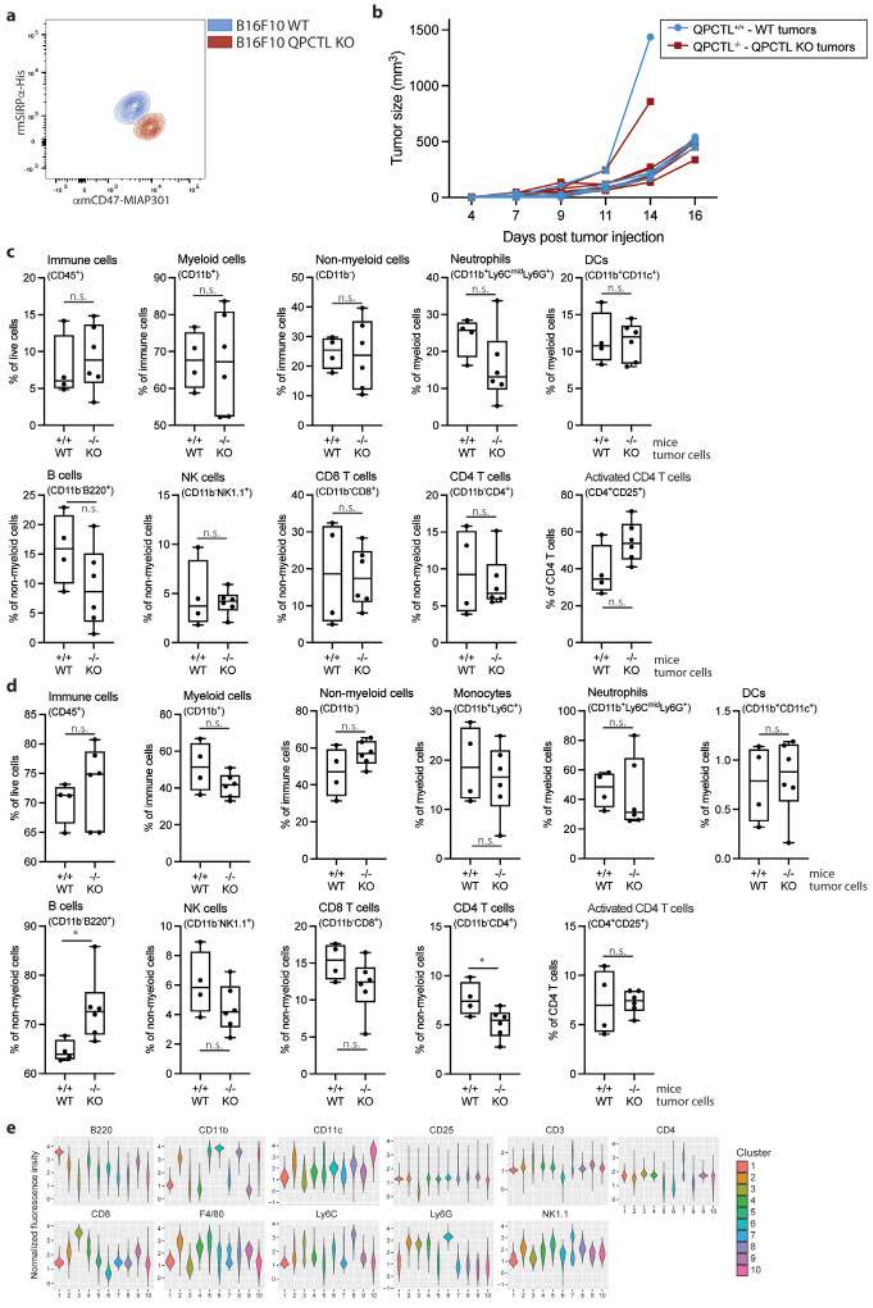

Extended Data Figure 2. Effect of QPCTL deficiency on the TME and blood cell compartment in tumor-bearing animals. a. Representative plot depicting rmSIRPα-His and amCD47 antibody (clone MIAP301) binding to B16F10 WT and B16F10 QPCTL KO cells, as measured by flow cytometry. **b.** Tumor growth in QPCTL$^{+/+}$ or QPCTL$^{-/-}$ mice inoculated with B16F10 WT and B16F10 QPCTL KO tumor cells, respectively. **c.** Frequency of immune cells (CD45^{+}) of live cells, myeloid (CD11b^{+}) and non-myeloid (CD11b^{-}) of immune cells, neutrophils (CD11b^{+}Ly6C^{mid}Ly6G^{+}) and DCs (CD11b^{+}CD11c^{+}) of my-

eloid cells, B cells ($CD11b^-B220^+$), NK cells ($CD11b^-NK1.1^+$), CD8 T cells ($CD11b^-CD8^+$) and CD4 T cells (CD11b-$CD4^+$) of non-myeloid cells, and activated CD4 T cells ($CD4^+CD25^+$) of total CD4 T cells, in the TME of $QPCTL^{+/+}$ (+/+) mice inoculated with B16F10 WT tumor cells and $QPCTL^{-/-}$ (-/-) mice inoculated with B16F10 QPCTL KO tumor cells. Data represent median ± min to max of individual mice. Dots depict immune cell frequency (%) or ratio (log_2) within individual mice. n = 4 ($QPCTL^{+/+}$) or n = 6 ($QPCTL^{-/-}$) mice per group. n.s., not significant by unpaired two-tailed t-test. **d.** Frequency of immune cells ($CD45^+$) of live cells, myeloid ($CD11b^+$) and non-myeloid ($CD11b^-$) of immune cells, monocytes (CD11b+$Ly6C^+$), neutrophils ($CD11b^+Ly6C^{mid}Ly6G^+$) and DCs ($CD11b^+CD11c^+$) of myeloid cells, B cells ($CD11b^-B220^+$), NK cells ($CD11b^-NK1.1^+$), CD8 T cells ($CD11b^-CD8^+$) and CD4 T cells ($CD11b^-CD4^+$) of non-myeloid cells, and activated CD4 T cells ($CD4^+CD25^+$) of total CD4 T cells, isolated in blood of $QPCTL^{+/+}$ (+/+) mice inoculated with B16F10 WT tumor cells and $QPCTL^{-/-}$ (-/-) mice inoculated with B16F10 QPCTL KO tumor cells. Data represent median ± min to max of individual mice. Dots depict immune cell frequency (%) or ratio (log_2) within individual mice. n = 4 ($QPCTL^{+/+}$) or n=6 ($QPCTL^{-/-}$) mice per group. *P =0.0404 (B cells); *P = 0.0405 (activated CD4 T cells); n.s., not significant, by unpaired two-tailed t-test. **e.** Violin plots depicting marker expression within the obtained clusters described in Fig. 2b. Data **a**-**e**) were obtained in a single experiment.

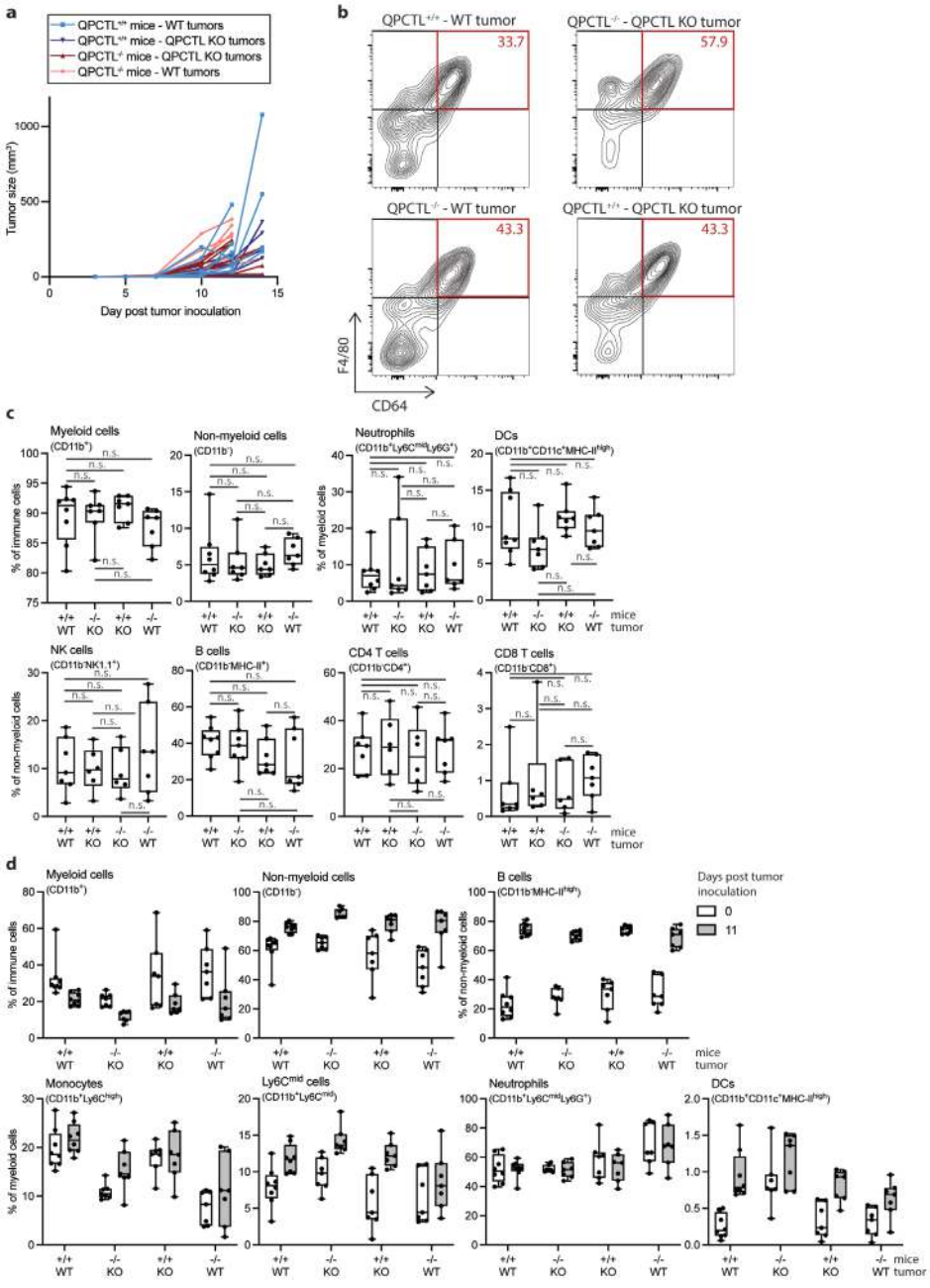

Extended Data Figure 3. Effect of QPCTL deficiency in tumor and host cell compartments. a. Tumor growth in QPCTL$^{+/+}$ mice inoculated with B16F10 WT or B16F10 QPCTL KO tumor cells, and in QPCTL$^{-/-}$ mice inoculated with B16F10 WT or B16F10 QPCTL KO tumor cells. **b.** Representative flow cytometry plots of data described in Fig. 2d, depicting macrophages (F4/80^{+}CD64^{+} cells) amongst total myeloid (CD11b^{+}) cells in the TME. Numbers depict the percentage macrophages within the myeloid cell gate. **c.** Frequency of myeloid (CD11b^{+}) and non-myeloid (CD11b^{-}) cells of immune cells, neutro-

phils ($CD11b^{+}Ly6C^{mid}Ly6G^{+}$) and DCs ($CD11b^{+}CD11c^{+}MHC\text{-}II^{high}$) of myeloid cells, and B cells ($CD11b^{-}MHC\text{-}II^{high}$), NK cells ($CD11b^{-}NK1.1^{+}$), CD4 T cells ($CD11b^{-}CD4^{+}$) and CD8 T cells ($CD11b^{-}CD8^{+}$) of non-myeloid cells, in the TME of $QPCTL^{+/+}$ mice inoculated with B16F10 WT or B16F10 QPCTL KO tumor cells, and $QPCTL^{-/-}$ mice inoculated with B16F10 WT or B16F10 QPCTL KO tumor cells. Data represent median ± min to max of individual mice. Dots represent immune cell frequency (%) within individual mice. *n* = 8 ($QPCTL^{+/+}$ with WT tumor cells) or *n* = 7 ($QPCTL^{-/-}$ with QPCTL KO tumor cells; $QPCTL^{+/+}$ with QPCTL KO tumor cells; $QPCTL^{-/-}$ with WT tumor cells) mice per group for myeloid cells, neutrophils, DCs, non-myeloid cells and B cells. *n* = 7 ($QPCTL^{+/+}$ with WT tumor cells; $QPCTL^{-/-}$ with WT tumor cells) or *n* = 6 ($QPCTL^{-/-}$ with QPCTL KO tumor cells; $QPCTL^{+/+}$ with QPCTL KO tumor cells) mice per group for NK cells, CD4 T cells and CD8 T cells. n.s., not significant by one-way ANOVA. **d.** Frequency of myeloid ($CD11b^{+}$) and non-myeloid ($CD11b^{-}$) cells of immune cells, and B cells ($CD11b^{-}MHC\text{-}II^{high}$) of non-myeloid cells, and Ly6C ^{mid} cells ($CD11b^{+}LyC6^{mid}$), neutrophils ($CD11b^{+}Ly6C^{mid}Ly6G^{+}$) and DCs ($CD11b^{+}CD11c^{+}MHC\text{-}II^{high}$) of myeloid cells, in blood of $QPCTL^{+/+}$ and $QPCTL^{-/-}$ mice before tumor inoculation (0 days), or 11 days after inoculation of B16F10 WT or QPCTL KO tumor cells. Data represent median ± min to max of individual mice. Dots represent immune cell frequency (%) within individual mice. *n* = 8 ($QPCTL^{+/+}$ with WT tumor cells) or *n* = 7 ($QPCTL^{-/-}$ with QPCTL KO tumor cells; $QPCTL^{+/+}$ with QPCTL KO tumor cells; $QPCTL^{-/-}$ with WT tumor cells) mice per group. Data in (a-c) depict single experiments, and are representative of 3 ($QPCTL^{+/+}$ with WT tumor cells and $QPCTL^{-/-}$ with QPCTL KO tumor cells groups) or 2 ($QPCTL^{+/+}$ with QPCTL KO tumor cells and $QPCTL^{-/-}$ with WT tumor cells groups) independent experiments with similar results. Data in **d**) were obtained in a single experiment.

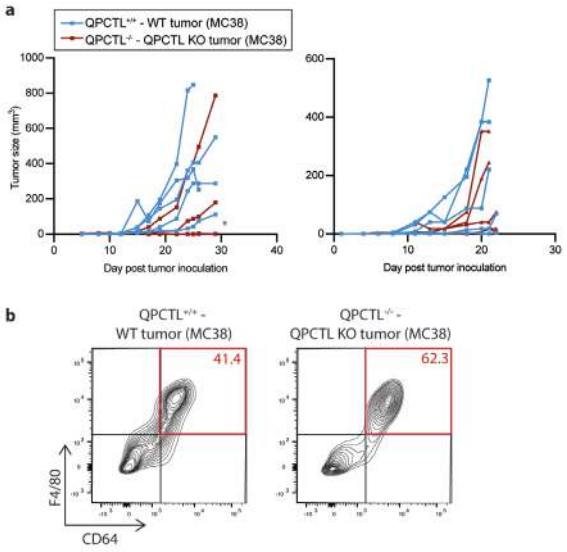

Extended Data Figure 4. Effect of QPCTL deficiency on TME composition. a. Tumor growth in QPCTL$^{+/+}$ mice inoculated with MC38 WT tumor cells and in QPCTL$^{-/-}$ mice inoculated with MC38 QPCTL KO tumor cells in two independent experiments. Asterisk (*) indicates impaired outgrowth of 3 MC38 QPCTL KO tumors in QPCTL$^{-/-}$ mice in one out of two experiments. **b.** Representative flow cytometry plots of data describe in **Fig. 2f**, depicting macrophages (F4/80^{+}CD64^{+} cells) amongst total myeloid (CD11b^{+}) cells in the TME. Numbers depict the percentage macrophages within the myeloid cell gate. Data in **a**) were obtained in 2 independent experiments and are both depicted.

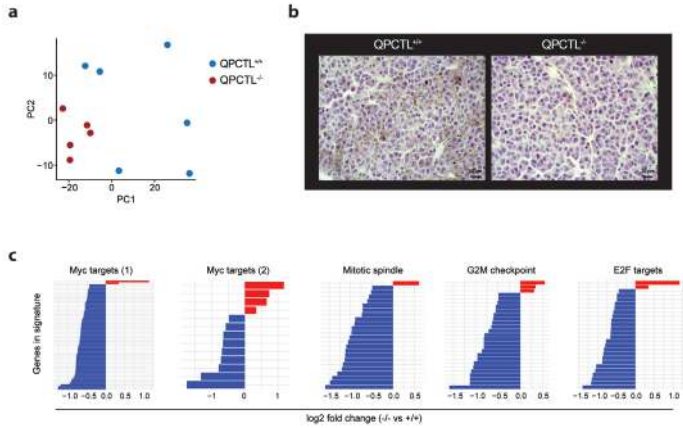

Extended Data Figure 5. Effect of QPCTL deficiency on tumor melanogenesis and proliferation. a. Principal component analysis performed on CD45$^-$ cells derived from QPCTL$^{+/+}$ ($n = 5$) and QPCTL$^{-/-}$ ($n = 6$) TMEs. **b.** Representative hematoxylin-eosin stained sections from QPCTL$^{+/+}$ and QPCTL$^{-/-}$ TMEs. Note the presence of melanin signal (brown) in the QPCTL$^{+/+}$ but not the QPCTL$^{-/-}$ sample. **c.** Waterfall plots depicting $\log_2$ fold change values of genes from indicated pathways obtained from MsigDB (Hallmark pathways). Data in **a**-**c**) are representative of at least 2 independent experiments. PC, principal component.

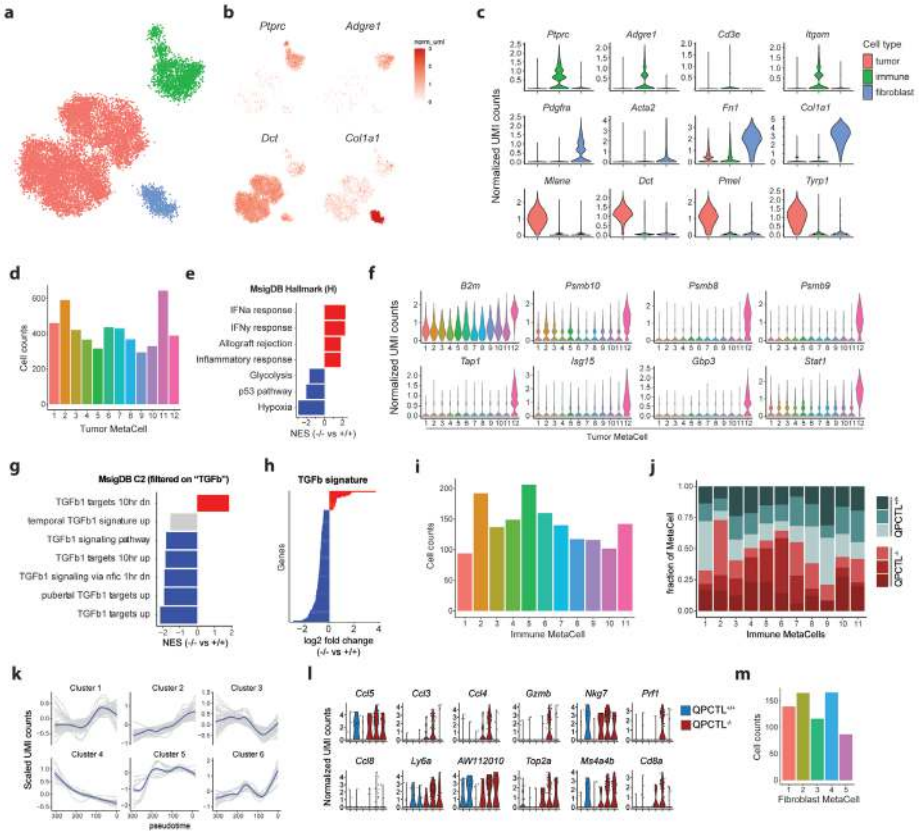

Extended Data Figure 6. Effect of QPCTL deficiency on tumor, immune and CAF subsets in the TME. a. 2-dimensional projection of MetaCell analysis of all cells obtained from QPCTL$^{+/+}$ (*n* = 3) and QPCTL$^{-/-}$ (*n* = 3) TMEs. Cells are colored by cell type, as defined in panel b-c). **b.** Normalized UMI counts of selected genes superimposed on 2-dimensional MetaCell projection. **c.** Violin plots depicting gene expression of selected cell type-specific genes within the major MC clusters obtained. **d.** Absolute cell counts per tumor cell MetaCell included in the analysis. **e.** Up- or downregulated Hallmark gene sets (MsigDB, H) identified through gene set enrichment analysis. Gene-sets with an FDR < 0.05 are shown, upregulated sets are shown in red, downregulated sets in blue. **f.** Normalized UMI counts of selected IFN responsive genes within each tumor MC. **g.** Up- and downregulated curated gene-sets (MsigDB, C2) identified through gene set enrichment analysis in the tumor cell compartment, only sets that contain the term 'TGFb' and with an FDR < 0.05 are depicted. **h.** Waterfall plot depicting log2 fold changes of TGFb responsive genes between QPCTL$^{-/-}$ and QPCTL$^{+/+}$ tumor cells obtained in Fig. 4e. **i.** Absolute cell counts per immune MetaCell included in the analysis. **j.** Sample composition of each immune MetaCell depicted as a stacked barchart. **k.** Gene clusters obtained through hierarchical clustering of gene expression kinetics across pseudotime. Graphs depict general additive models fitted for each gene in grey. Blue lines represent average trends for each cluster. **l.** Top 12 genes with the highest relative expression in CD3^{+} lymphocytes (MC6) from QPCTL$^{-/-}$ TMEs (red, *n* = 3) as compared to QPCTL$^{+/+}$ TMEs (blue, *n* = 3). Violin plots depicting normalized UMI counts. **m.** Absolute cell counts per fibroblast MetaCell included in the analysis.

Data in **a**-**m**) represent data acquired from 6 individual TMEs (3 QPCTL$^{+/+}$; 3 QPCTL$^{-/-}$) obtained in a single experiment.

iCAF	myCAF
Clec3b	*Spp1*
Gsn	*Serpine2*
Ptx3	*Cxcl14*
Ly6c1	*Crlf1*
Efemp1	*Igfbp3*
Ly6a	*Acta2*
Figf	*Tagln*
Tnfaip6	*Thy1*
Ifi27l2a	*Col8a1*
Dpt	*Cthrc1*
Adm	*Sfrp1*
Plpp3	*Tnc*
Tnxb	*Sparcl1*
Cxcl12	*Col15a1*
Gstm1	*Col12a1*
C4b	*Tgfb1*
Ogn	*Col1a1*
C3	*Sdc1*
Pcolce2	*Cilp*
Cxcl1	*H19*
Col14a1	*Thbs2*
Svep1	
Adamts5	
Hp	
Has1	
Scara3	
Ifi205	
Dpep1	
Sfrp4	
Prss23	
Ackr3	
Htra3	
Apoe	
Ccl7	
Il6	
Sfrp2	
Pla1a	
Scara5	
Sned1	

Supplementary Table 1. iCAF and myCAF signature genes.

Antibodies	Company	Catalog number
7-AAD Viability Staining Solution	ThermoFisher	00-6993-50
anti-His tag APC (J095G46)	Biolegend	362605
anti-mouse B220 BUV737 (RA3-6B2)	BD Biosciences	612839
anti-mouse CD11b BV786 (M1/70)	BD Biosciences	740861
anti-mouse CD11c PE-CF594 (HL3)	BD Biosciences	562454
anti-mouse CD11c PE-Cy5 (N418)	Biolegend	117316
anti-mouse CD137 BV510 (1AH2)	BD Biosciences	740134
anti-mouse CD16/32 (S17011E)	Biolegend	156604
anti-mouse CD25 PE (PC61)	Biolegend	102007
anti-mouse CD279 PE-Cy7 (J43)	Invitrogen	25-9985-82
anti-mouse CD3e FITC (145-2C11)	Invitrogen	11-0031-85
anti-mouse CD4 APC (GK1.5)	Invitrogen	17-0041-83
anti-mouse CD4 BUV805 (RM4-4)	BD Biosciences	741913
anti-mouse CD44 APC/Cy7 (IM7)	Biolegend	103027
anti-mouse CD45 AF488 (30-F11)	Biolegend	103122
anti-mouse CD45 BUV395 (30-F11)	BD Biosciences	564279
anti-mouse CD47 PE (miap301)	Biolegend	127508
anti-mouse CD64 BV421 (X54-5/7.1)	Biolegend	139309
anti-mouse CD8a PerCP-Cy 5.5 (53-6.7)	BD Pharmingen	551162
anti-mouse F4/80 PE (T45-2342)	BD Pharmingen	565410
anti-mouse I-A/I-E PE/Cy7 (M5/114.15.2)	Biolegend	107640
anti-mouse Ly6C BV605 (HK1.4)	Biolegend	128035
anti-mouse Ly6G AF700 (1A8)	Biolegend	127622
anti-mouse NK1.1 PE/Cy7 (PK136)	Biolegend	108714
anti-mouse/human Langerin (4C7)	Biolegend	144206

Supplementary Table 2. Antibodies used to analyze immune cells in tumor single cell suspensions

REFERENCES

1. Rumpret, M. *et al.* Functional categories of immune inhibitory receptors. *Nat Rev Immunol* **20**, 771–780 (2020).
2. Jaiswal, S. *et al.* CD47 Is Upregulated on Circulating Hematopoietic Stem Cells and Leukemia Cells to Avoid Phagocytosis. *Cell* **138**, 271–285 (2009).
3. Majeti, R. *et al.* CD47 Is an Adverse Prognostic Factor and Therapeutic Antibody Target on Human Acute Myeloid Leukemia Stem Cells. *Cell* **138**, 286–299 (2009).
4. Zhao, X. W. *et al.* CD47–signal regulatory protein-α (SIRPα) interactions form a barrier for antibody-mediated tumor cell destruction. *Proc National Acad Sci* **108**, 18342–18347 (2011).
5. Cynis, H. *et al.* Isolation of an Isoenzyme of Human Glutaminyl Cyclase: Retention in the Golgi Complex Suggests Involvement in the Protein Maturation Machinery. *J Mol Biol* **379**, 966–980 (2008).
6. Logtenberg, M. E. W. *et al.* Glutaminyl cyclase is an enzymatic modifier of the CD47- SIRPα axis and a target for cancer immunotherapy. *Nat Med* **25**, 612–619 (2019).
7. Schilling, S. *et al.* Identification of Human Glutaminyl Cyclase as a Metalloenzyme POTENT INHIBITION BY IMIDAZOLE DERIVATIVES AND HETEROCYCLIC CHELATORS*. *J Biol Chem* **278**, 49773–49779 (2003).
8. Stephan, A. *et al.* Mammalian glutaminyl cyclases and their isoenzymes have identical enzymatic characteristics. *Febs J* **276**, 6522–6536 (2009).
9. Hatherley, D. *et al.* Paired Receptor Specificity Explained by Structures of Signal Regulatory Proteins Alone and Complexed with CD47. *Mol Cell* **31**, 266–277 (2008).
10. Cynis, H. *et al.* The isoenzyme of glutaminyl cyclase is an important regulator of monocyte infiltration under inflammatory conditions. *Embo Mol Med* **3**, 545–558 (2011).
11. Chen, Y.-L. *et al.* Inhibition of glutaminyl cyclase attenuates cell migration modulated by monocyte chemoattractant proteins. *Biochem J* **442**, 403–412 (2012).
12. Kehlen, A. *et al.* N-terminal pyroglutamate formation in CX3CL1 is essential for its full biologic activity. *Bioscience Rep* **37**, (2017).
13. Mair, B. *et al.* High-throughput genome-wide phenotypic screening via immunomagnetic cell sorting. *Nat Biomed Eng* **3**, 796–805 (2019).
14. Becker, A. *et al.* IsoQC (QPCTL) knock-out mice suggest differential substrate conversion by glutaminyl cyclase isoenzymes. *Biol Chem* **397**, 45–55 (2016).
15. Schepsky, A. *et al.* The microphthalmia-associated transcription factor Mitf interacts with beta-catenin to determine target gene expression. *Mol Cell Biol* **26**, 8914–27 (2006).
16. Cho, M. *et al.* Cardamonin suppresses melanogenesis by inhibition of Wnt/beta-catenin signaling. *Biochem Bioph Res Co* **390**, 500–5 (2009).
17. Luo, X. *et al.* The tumor suppressor interferon regulatory factor 8 inhibits β-catenin signaling in breast cancers, but is frequently silenced by promoter methylation. *Oncotarget* **8**, 48875–48888 (2017).
18. Bai, M. *et al.* The crosstalk between β-catenin signaling and type I, type II and type III interferons in lung cancer cells. *Am J Transl Res* **9**, 2788–2797 (2017).
19. Nava, P. *et al.* IFNγ-induced suppression of β-catenin signaling: evidence for roles of Akt and 14.3.3ζ. *Mol Biol Cell* **25**, 2894–2904 (2014).
20. Baran, Y. *et al.* MetaCell: analysis of single-cell RNA-seq data using K-nn graph partitions. *Genome Biol* **20**, 206 (2019).

21. Zimmerman, K. A. *et al.* Single-Cell RNA Sequencing Identifies Candidate Renal Resident Macrophage Gene Expression Signatures across Species. *J Am Soc Nephrol Jasn* **30**, 767–781 (2019).
22. Qian, J. *et al.* A pan-cancer blueprint of the heterogeneous tumor microenvironment revealed by single-cell profiling. *Cell Res* **30**, 745–762 (2020).
23. Mattiola, I. *et al.* The macrophage tetraspan MS4A4A enhances dectin-1-dependent NK cell-mediated resistance to metastasis. *Nat Immunol* **20**, 1012–1022 (2019).
24. Bowman, R. L. *et al.* Macrophage Ontogeny Underlies Differences in Tumor-Specific Education in Brain Malignancies. *Cell Reports* **17**, 2445–2459 (2016).
25. Arlauckas, S., Oh, N., Li, R., Weissleder, R. & Miller, M. A. Macrophage imaging and subset analysis using single-cell RNA sequencing. *Nanotheranostics* **5**, 36–56 (2021).
26. Cheng, S. *et al.* A pan-cancer single-cell transcriptional atlas of tumor infiltrating myeloid cells. *Cell* **184**, 792-809.e23 (2021).
27. Chen, Y.-J. *et al.* Eps8 Protein Facilitates Phagocytosis by Increasing TLR4-MyD88 Protein Interaction in Lipopolysaccharide-stimulated Macrophages. *J Biol Chem* **287**, 18806–18819 (2012).
28. Fan, W. *et al.* ECM1 Prevents Activation of Transforming Growth Factor β, Hepatic Stellate Cells, and Fibrogenesis in Mice. *Gastroenterology* **157**, 1352-1367.e13 (2019).
29. Huang, S. C.-C. *et al.* Cell-intrinsic lysosomal lipolysis is essential for alternative activation of macrophages. *Nat Immunol* **15**, 846–55 (2014).
30. Yu, T. *et al.* Modulation of M2 macrophage polarization by the crosstalk between Stat6 and Trim24. *Nat Commun* **10**, 4353 (2019).
31. Mhaidly, R. & Mechta-Grigoriou, F. Fibroblast heterogeneity in tumor micro-environment: Role in immunosuppression and new therapies. *Semin Immunol* **48**, 101417 (2020).
32. Öhlund, D. *et al.* Distinct populations of inflammatory fibroblasts and myofibroblasts in pancreatic cancer. *J Exp Med* **214**, 579–596 (2017).
33. Elyada, E. *et al.* Cross-Species Single-Cell Analysis of Pancreatic Ductal Adenocarcinoma Reveals Antigen-Presenting Cancer-Associated Fibroblasts. *Cancer Discov* **9**, 1102–1123 (2019).
34. Jimenez-Sanchez, M. *et al.* siRNA screen identifies QPCT as a druggable target for Huntington's disease. *Nat Chem Biol* **11**, 347–354 (2015).
35. Lues, I. *et al.* A phase 1 study to evaluate the safety and pharmacokinetics of PQ912, a glutaminyl cyclase inhibitor, in healthy subjects. *Alzheimer's Dementia Transl Res Clin Interventions* **1**, 182–195 (2015).
36. Arwert, E. N. *et al.* A Unidirectional Transition from Migratory to Perivascular Macrophage Is Required for Tumor Cell Intravasation. *Cell Reports* **23**, 1239–1248 (2018).
37. Qian, B.-Z. *et al.* CCL2 recruits inflammatory monocytes to facilitate breast-tumour metastasis. *Nature* **475**, 222–225 (2011).
38. Tymoszuk, P. *et al.* In situ proliferation contributes to accumulation of tumor-associated macrophages in spontaneous mammary tumors. *Eur J Immunol* **44**, 2247–2262 (2014).
39. Laouar, Y., Sutterwala, F. S., Gorelik, L. & Flavell, R. A. Transforming growth factor-β controls T helper type 1 cell development through regulation of natural killer cell interferon-γ. *Nat Immunol* **6**, 600–607 (2005).
40. Tauriello, D. V. F. *et al.* TGFβ drives immune evasion in genetically reconstituted colon cancer metastasis. *Nature* **554**, 538–543 (2018).
41. Mariathasan, S. *et al.* TGFβ attenuates tumour response to PD-L1 blockade by contributing to exclusion of T cells. *Nature* **554**, 544–548 (2018).
42. Kieffer, Y. *et al.* Single-Cell Analysis Reveals Fibroblast Clusters Linked to Immunotherapy Resistance in Cancer. *Cancer Discov* **10**, 1330–1351 (2020).

43. Dominguez, C. X. *et al.* Single-Cell RNA Sequencing Reveals Stromal Evolution into LRRC15+ Myofibroblasts as a Determinant of Patient Response to Cancer Immunotherapy. *Cancer Discov* **10**, 232–253 (2020).
44. Brinkman, E. K., Chen, T., Amendola, M. & Steensel, B. van. Easy quantitative assessment of genome editing by sequence trace decomposition. *Nucleic Acids Res* **42**, e168 (2014).
45. Hahne, F. *et al.* flowCore: a Bioconductor package for high throughput flow cytometry. *Bmc Bioinformatics* **10**, 106 (2009).
46. Kim, D., Paggi, J. M., Park, C., Bennett, C. & Salzberg, S. L. Graph-based genome alignment and genotyping with HISAT2 and HISAT-genotype. *Nat Biotechnol* **37**, 907–915 (2019).
47. Robinson, M. D., McCarthy, D. J. & Smyth, G. K. edgeR: a Bioconductor package for differential expression analysis of digital gene expression data. *Bioinform Oxf Engl* **26**, 139–40 (2009).
48. Hao, Y. *et al.* Integrated analysis of multimodal single-cell data. *Cell* **184**, 3573-3587.e29 (2021).
49. Street, K. *et al.* Slingshot: cell lineage and pseudotime inference for single-cell transcriptomics. *Bmc Genomics* **19**, 477 (2018).
50. Berge, K. V. den *et al.* Trajectory-based differential expression analysis for single-cell sequencing data. *Nat Commun* **11**, 1201 (2020).